International Journal of Plasticity 151 (2022) 103219

Contents lists available at ScienceDirect

International Journal of Plasticity

journal homepage: www.elsevier.com/locate/ijplas

Modelling stress relaxation after hot deformation: Microstructure-property relationships in Nb-bearing steels

Jianwei Zhao [a,b], Quan Yang [a,b], Hossein Eskandari Sabzi [c], Wei Wen [c], Pedro E. J. Rivera-Díaz-del-Castillo [c,*]

[a] Institute of Engineering Technology, University of Science and Technology Beijing, Beijing 100083, China
[b] National Engineering Research Center of Flat Rolling Equipment, University of Science and Technology Beijing, Beijing 100083, China
[c] Department of Engineering, Engineering Building, Lancaster University, LA1 4YW, United Kingdom

ARTICLE INFO

Keywords:
Stress relaxation
Recovery
Recrystallization
Additive manufacturing
Multi-pass metal forming

ABSTRACT

Stress relaxation taking place after hot deformation is modelled by incorporating the simultaneous action of various physical phenomena. Dislocation recovery, recrystallization, and precipitation are all interrelated adopting new formulations. Dislocation recovery is approached through a vacancy-mediated dislocation climb approach. Recrystallization is considered to be meta-dynamic or static, and the effects of precipitate pinning and (interstitial and substitutional) solute drag are incorporated. The kinetics of precipitation nucleation, growth, and coarsening are also taken into account; precipitate nucleation in dislocation cells is assumed and thus the dislocation cell evolution is accounted for. The softening behaviour is thus tracked for 6 micro-alloyed steel grades and compared with 37 softening curves for a range of temperatures and prior deformation rates; the modelling describes the experiments with great accuracy. The application of the approach to additive manufacturing microstructural relaxation is discussed.

1. Introduction

Stress relaxation caused by microstructural evolution after hot deformation in metals is of great technological importance as the mechanical properties and residual stress in the product are severely changed. For multi-pass metal thermal forming processes such as forging and rolling, and more recently for additive manufacturing, it is necessary to predict the evolution of mechanical properties and residual stress (Brown and Bammann, 2012; Li et al., 2020; Liu et al., 2020). In wrought products, such changes follow work hardening in deformation passes; for additive manufacturing, the quick cycles of heating and cooling impose thermal strains upon layering. The control of these changes is vital to ensure the dimensional accuracy and mechanical properties of the product. For instance, in hot-strip rolling the accurate estimation of the rolling force and residual stress to precisely control the thickness and shape of the strip is only possible when the softening processes between stands are accurately described (Zhao et al., 2018). Thus, to computationally optimise manufacturing processes it is necessary to provide a model that captures the multiple physical mechanisms behind stress relaxation. Such a model would allow to comprehensively understand the relation among the thermo-mechanical processing, microstructure, and material properties, as well as their influences in residual stress development, so as to promote a reduction in time and cost for developing products with better performance during the design stage (Min et al., 2020).

* Corresponding author.
E-mail address: p.rivera1@lancaster.ac.uk (P.E.J. Rivera-Díaz-del-Castillo).

https://doi.org/10.1016/j.ijplas.2022.103219
Received 23 August 2021; Received in revised form 18 November 2021;
Available online 13 January 2022

The microstructure evolution after hot deformation is a complex metallurgical process involving multiple physical phenomena. Generally, as shown in Fig. 1, the material after deformation at elevated temperatures will undergo processes of recovery, static recrystallization and grain growth, leading to a classical static recrystallization process. If dynamic recrystallization is triggered upon deformation, meta-dynamic recrystallization will replace the static recrystallization shown in Fig. 1. Except for the absence of an incubation time (t_c) in the meta-dynamic recrystallization, the microstructure evolution of both meta-dynamic and static recrystallization is similar (Humphreys and Hatherly, 2012). Concomitantly, the nucleation, growth and coarsening of precipitates will take place; the effect of solute atoms pinning grain boundary motion will also be present.

Significant effort has been put into modelling individually each basic physical process mentioned above (Dutta et al., 2001; He et al., 2017; Martınez-de-Guerenu et al., 2004; Min et al., 2020; Song et al., 2001; Svoboda et al., 2011; Verdier et al., 1998): recovery, static and meta-dynamic recrystallization, precipitation and solute drag. Although previous work has proposed models by coupling some of these processes (Bäcke, 2010; Buken and Kozeschnik, 2017; Engberg and Lissel, 2008; Li et al., 2009; Zeng et al., 2019; Zurob et al., 2002), there is currently no model combining all such processes simultaneously; this would allow to accurately predict microstructural evolution during and after hot deformation. Most of the related work (Brown and Bammann, 2012; Cho et al., 2019; Tang et al., 2020; Zurob et al., 2002) focus on the evolution of static recrystallization volume fraction which evaluate the softening behaviour of deformed material by a simple mixture rule based on the volume fraction. The effect of precipitates has been estimated by adding the Zener pressure in the driving force for recrystallization, and the solute drag effect is described by altering the grain boundary mobility. Zurob et al. (2002) have developed such type of model coupling recovery, static recrystallization and precipitation, and Tang et al. (2020) further applied it to model static softening mechanisms for multi-stage hot deformation in Al-Zn-Mg-Cu alloys. Although such methods provide a description of softening behaviour of the deformed material, empirical and phenomenological relations are introduced together with material-dependent fitting parameters, restricting their extension to new or more complex systems. Moreover, the description of both meta-dynamic and static recrystallization under the same formulation has not yet been achieved.

A key aspect of the modelling approach adopted here is the use of the thermostatistical theory of plasticity. Such approach combines dislocation multiplication and annihilation with thermodynamic variables such as temperature and composition; additionally, it allows to naturally incorporate strain rate. The approach is based on the principle that, when a deformation process occurs, dislocations can glide a number of lattice spaces only limited by the speed of sound in the material (Galindo-Nava et al., 2012). However, the most likely dislocation glide configuration is determined by energy balance. The approach has been extended to dislocation cell formation (Galindo-Nava and Rivera-Díaz-del-Castillo, 2012) and to dynamic recovery and recrystallization (Galindo-Nava and Rivera-Díaz-del-Castillo, 2013). Dislocation cells are treated as minimum energy configurations with misorientation and size allowing the uptake of further deformation. Recrystallized structures are dealt with as dislocation rearrangements, where moving boundaries swipe across the microstructure reducing strain energy of heavily dislocated regions. A key aspect of the thermostatistical plasticity theory is the capacity to incorporate composition, which prevents the need for composition-dependent fitting parameters. The corresponding detailed equations are introduced in the modelling section.

The purpose of the model presented here is to provide a quantitative description of the interaction between the microstructure

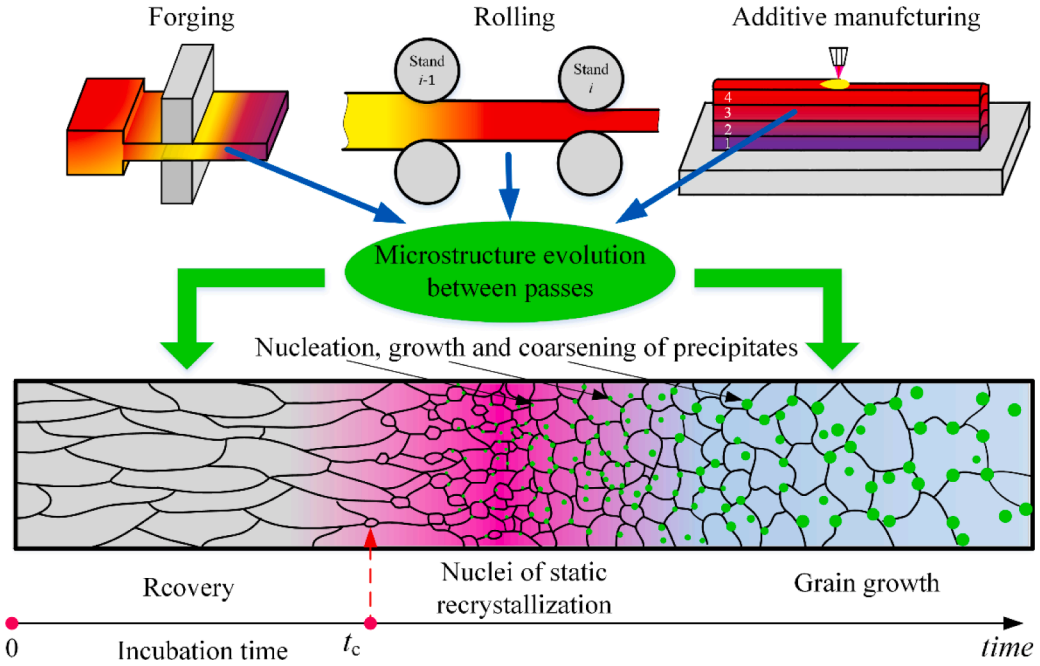

Fig. 1. Microstructure evolution: phases and deformation structures.

evolution and the stress relaxation *after* hot deformation. A new description for the overall dislocation density evolution after hot deformation is presented; this incorporates, for the first time, expressions for the softening effect due to recovery and post-deformation recrystallization, which incorporate formulations for dislocation density decrease. The multiple post-deformation physical metallurgical mechanisms underwent by the material such as recovery, recrystallization, solute drag, and precipitation (Doherty et al., 1997) were incorporated in the current approach. By coupling their interaction, as illustrated in Fig. 2, a model was established uniquely combining kinetic and thermostatistical approaches incorporating the average dislocation density as a core state variable (Bammann and Solanki, 2010; Galindo-Nava and Rivera-Díaz-del-Castillo, 2013, 2014; Puchi-Cabrera et al., 2014).

Compared to previous work, the model developed here can be distinguished by the following novel features:

(1) The description of the overall dislocation density evolution after hot deformation directly incorporates the contributions from all physical phenomena. Traditional approaches calculate instead the recrystallization volume fraction and estimate the overall dislocation density by a weighted average of the non-recrystallized and recrystallized regions.
(2) The model is based on kinetic and thermostatistical approaches incorporating several physical parameters, including temperature and chemical composition. This circumvents the need in previous work for fitting composition-dependent parameters, such as the activation energy and Avrami constants in phenomenological models.
(3) An expression for the post-deformation recrystallization coefficient is proposed to quantify the capability for recrystallized grains to grow and occupy deformed regions. Such expression is formulated in terms of the statistical dislocation entropy after hot deformation; the drag energy of niobium and the pinning energy of precipitates are also taken into account.
(4) An expression for the precipitate number density is proposed assuming a random particle distribution at subgrain boundaries.
(5) The average subgrain boundary pinning energy due to precipitation was derived.
(6) An expression for the critical subgrain size for static recrystallization is derived from energy balance based on the thermostatistical plasticity theory. Such expression incorporates the effects of composition, precipitation and solute drag, making the calculation of critical subgrain size more robust and adaptable. In contrast, traditional approaches adopt a fixed grain boundary energy that is often fitted.

The approach developed in this work is applied to metal thermal forming processing, accurately predicting the stress relaxation process coupling the multiple physical mechanisms in a broad range of steel grades and deformation conditions. This work is in sections: the details for modelling, including the aforementioned unique approaches, are presented in Section 2. The selection of parameters and the validation of the model are described in Section 3. Section 4 is the discussion and Section 5 presents concluding remarks.

2. Model

The softening of metals after hot deformation is a complex process due to the simultaneous activation of a range of metallurgical processes; these include static recovery, post-deformation recrystallization, solute drag and precipitation, which influence each other. Softening can be described in terms of a decaying average dislocation density. Given that static recovery and post-deformation recrystallization are the main contributions to softening, the evolution of the average dislocation density is proposed:

$$\frac{\mathrm{d}\rho(t)}{\mathrm{d}t} = -f_{\mathrm{SRV}}\rho(t) - f_{\mathrm{RX}}\rho(t) \tag{1}$$

where t is time, f_{SRV} is the static recovery coefficient, f_{RX} is the post-deformation recrystallization coefficient and ρ is the average dislocation density. The effects of solute drag and precipitation are introduced as described in subsequent sections. Adopting the Taylor

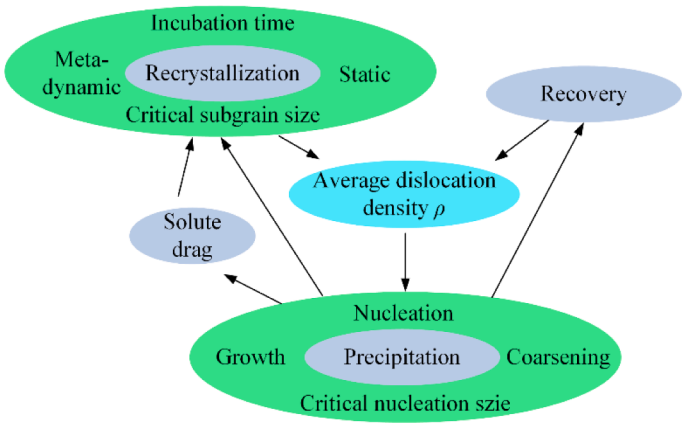

Fig. 2. Relationship among physical metallurgical processes.

relation (Bailey and Flanagan, 1967; Kassner, 2018), the stress relaxation process can be described based on the evolution of the average dislocation density obtained from solving Eq. (1):

$$\sigma = \sigma_0 + \alpha\mu M b\sqrt{\rho} \tag{2}$$

where σ_0 is the steady state stress, $\alpha = 0.3$ is a dislocation–dislocation interaction coefficient (Martınez-de-Guerenu et al., 2004; Verdier et al., 1998), μ is the shear modulus, $M = 3.1$ is the Taylor factor (Bäcke, 2010; Zurob et al., 2002) and b is the magnitude of the Burgers vector.

2.1. Static recovery

As the displacement of dislocations occurs, annihilation takes place when dislocations of antiparallel Burgers vector meet, with the rate of annihilation depending on the (waiting) time for such encounter to take place. Correspondingly, the static recovery coefficient f_{SRV} can be defined as the frequency of annihilation, i.e. $f_{SRV} = 1/t_w$, where t_w is the average waiting time. Based on this idea, the approach given by Huang et al. (2011) is adopted to calculate t_w. Its underlying physical idea is to assume that edge dislocation climb is the main mechanism of recovery at high temperature, and that two dislocations of opposite sign forming a dipole edge dislocation configuration will meet as a result of the climb. The average waiting time $t_w = h_d/v_c$ is calculated from the average distance h_d for dislocations to move before annihilation and the velocity v_c of the edge dislocation climb; h_d is assumed to be equal to the average distance $\bar{l} = 1/\sqrt{\rho}$ between dislocations. When the velocity of the edge dislocation climb is expressed as (Huang et al., 2011):

$$v_c = 2n_c b^2 \vartheta_D \sqrt{\rho_0} \exp\left(-\frac{\left(\sqrt{\rho_0} - \sqrt{\rho}\right)\xi\mu b^4}{kT}\right)\exp\left(-\frac{U_{SRV}}{RT}\right)\left[\exp\left(\frac{\sqrt{\rho}\xi\mu b^4}{kT}\right) - 1\right] \tag{3}$$

the static recovery coefficient can be derived:

$$f_{SRV} = 2n_c b^2 \vartheta_D \sqrt{\rho_0} \exp\left(-\frac{\left(\sqrt{\rho_0} - \sqrt{\rho}\right)\xi\mu b^4}{kT}\right)\exp\left(-\frac{U_{SRV}}{RT}\right)\left[\exp\left(\frac{\sqrt{\rho}\xi\mu b^4}{kT}\right) - 1\right]\sqrt{\rho} \tag{4}$$

Where n_c is the number of nearest neighbours for diffusion (~11 for face-centred cubic metals (Argon and Moffatt, 1981)), ϑ_D is the Debye frequency, ρ_0 is the initial dislocation density after hot deformation ($t = 0$), ξ is the stress intensity factor, U_{SRV} is the recovery activation energy, T is the absolute temperature, k is the Boltzmann constant and R is the ideal gas constant.

2.2. Precipitation

2.2.1. Precipitation modelling

Precipitation after hot deformation is modelled by integrating nucleation, growth, and coarsening (Deschamps and Brechet, 1998; Dutta et al., 2001; Mukherjee et al., 2014; Perez et al., 2008; Perrard et al., 2007). The assumption followed by Perrard et al. (2007), and Dutta and Sellars (1987), that the nucleation of precipitates after hot deformation only occurs on dislocations, is followed here. The precipitation incubation time is ignored (Dutta et al., 2001; Zurob et al., 2002). Correspondingly, the changes in Gibbs energy $\Delta G(Rp)$ associated with the formation of a precipitate in a supersaturated solid solution is estimated as (Okaguchi and Hashimoto, 1992; Zurob et al., 2001, 2002):

$$\Delta G(R_p) = \frac{4}{3}\pi R_p^3 \Delta G_v + 4\pi R_p^2 \gamma - \frac{\ln(R_p/b)}{2\pi(1-\nu)}\mu b^2 R_p - \frac{1}{5}\mu b^2 R_p \tag{5}$$

where the first term on the right-hand side represents the chemical free energy, the second term represents the interfacial free energy, and the last two terms stand for the increase in elastic energy due to dislocations decorated by spherical precipitates of radius R_p; ν is the Poisson's ratio, γ is the interphase energy per unit area and ΔGv is the chemical driving force for precipitation. For the NbC precipitate, $\Delta G_v = -\frac{RT}{V_m}\ln\frac{C_{Nb}C_C}{C_{Nb}^e C_C^e}$ (Dutta et al., 2001; Perrard et al., 2007), where v_m is the molecular volume of NbC, C_{Nb} and C_C are the instantaneous concentrations of Nb and C in mole fraction in the matrix, while C_{Nb}^e and C_C^e are the equilibrium concentrations in the matrix as determined from the solubility product K_s at the annealing temperature. The classical expression for the critical nucleation radius $R_{pc} = -2\gamma/\Delta G_v$ (Dutta et al., 2001) is substituted into Eq. (5) to calculate the energy barrier for precipitate nucleation. This expression only incorporates the chemical free energy and the interfacial free energy; the effect of dislocation strain on precipitate nucleation is not accounted for. Based on the classical nucleation theory, the critical radius for nucleation in this approach corresponds to the maximum value ΔG^* of the Gibbs energy $\Delta G(R_p)$ (Maugis and Gouné, 2005; Perez et al., 2008), thus, R_{pc} can be calculated from:

$$\frac{\partial \Delta G(R_p)}{\partial R_p} = 0 \tag{6}$$

Then, by substituting the critical radius into Eq. (5), the maximum value of the Gibbs energy, i.e. the energy barrier for nucleation, can be obtained from $\Delta G^* = \Delta G(R_{pc})$. Then, the nucleation rate is obtained as (Dutta et al., 2001; Zurob et al., 2002):

$$\frac{dN}{dt}\Big|_{\text{nucleation}} = (N_0 - N)Z\beta\exp\left(-\frac{\Delta G^*}{kT}\right) \tag{7}$$

where N is the number of precipitates per unit volume, N_0 is the initial number of available nucleation sites per unit volume which is proportional to the number of substitutional sites on dislocations per unit volume (Perrard et al., 2007; Zurob et al., 2002), i.e. $N_0 = F\rho/b$, where F is a proportionality constant; Z is the Zeldovich factor, β is the critical solute attachment rate; according to the derivation of Russell (Russell, 1980), $Z\beta$ can be approximated as $Z\beta = D_{\text{pipe}}C_{\text{Nb}}/a^2$, where D_{pipe} is the pipe diffusion coefficient and a is the lattice spacing.

To describe the average precipitate growth rate during the nucleation-growth stage, the classical Zener equation (Zener, 1949) for growth rate is modified as (Deschamps and Brechet, 1998; Dutta et al., 2001):

$$\frac{dR_p}{dt}\Big|_{\text{growth}} = \frac{D_{\text{bulk}}}{R_p}\cdot\frac{C_{\text{Nb}} - C^e_{\text{Nb}}\exp(R_0/R_p)}{C^p_{\text{Nb}} - C^e_{\text{Nb}}\exp(R_0/R_p)} + \frac{1}{N}\frac{dN}{dt}(\varphi R_{pc} - R_p) \tag{8}$$

The first term on the right-hand side accounts for the growth of existing precipitates and the second term accounts for the effect of new nuclei on the average radius. Where D_{bulk} is the bulk diffusivity of solute atoms in the austenite, which will be replaced by an effective diffusion coefficient D_{eff} to account for the effect of pipe diffusion through dislocation cores on growth when precipitates nucleate on dislocations (Medina et al., 2020; Mukherjee et al., 2014; Zurob et al., 2002), and the effective diffusion coefficient is calculated from the weighted mean of the bulk diffusion and pipe diffusion coefficients $D_{\text{eff}} = D_{\text{pipe}}\pi R^2_{\text{core}}\rho + D_{\text{bulk}}(1 - \pi R^2_{\text{core}}\rho)$ (Dutta et al., 2001), where R_{core} is the radius of the dislocation core; C^p_{Nb} is the concentration of Nb in the precipitate; R_0 is a capillarity radius calculated by $R_0 = R_{pc}\ln(C_{\text{Nb}}/C^e_{\text{Nb}})$ (Deschamps and Brechet, 1998); φ is a factor to account for the fact that the nucleated precipitates should be slightly larger than the critical radius to ensure a stable growth, and the value $\varphi = 1.05$ (Deschamps and Brechet, 1998; Dutta et al., 2001) is adopted.

As the supersaturation of solute in solid solution decreases during the nucleation-growth stage, the critical radius for precipitate nucleation will continuously increase. When the critical radius of precipitates nearly becomes equal to the mean radius, the coarsening stage begins. During coarsening, larger particles grow at the expense of their smaller counterparts, resulting in an increase in the mean radius and a decrease in the precipitate number density. Correspondingly, the precipitate coarsening rate and the evolution of precipitate number density are described from (Dutta et al., 2001):

$$\frac{dR_p}{dt}\Big|_{\text{coarsening}} = \frac{4}{27}\frac{C^e_{\text{Nb}}}{C^p_{\text{Nb}} - C^e_{\text{Nb}}}\cdot\frac{R_0 D_{\text{eff}}}{R_p^2} \tag{9}$$

$$\frac{dN}{dt}\Big|_{\text{coarsening}} = \frac{4}{27}\frac{C^e_{\text{Nb}}}{C^p_{\text{Nb}} - C^e_{\text{Nb}}}\cdot\frac{R_0 D_{\text{eff}}}{R_p^3}\left[\frac{R_0 C_{\text{Nb}}}{R_p(C^p_{\text{Nb}} - C_{\text{Nb}})}\left(\frac{3}{4\pi R_p^3} - N\right) - 3N\right] \tag{10}$$

In order to track the transition from growth to the coarsening stage, a coarsening fraction $F_c = 1 - \text{erf}\left[4\left(\frac{R_p}{R_{pc}} - 1\right)\right]$ is introduced by Deschamps and Brechet (Deschamps and Brechet, 1998) to provide an overall description of the evolution of the precipitate radius:

$$\frac{dR_p}{dt} = (1 - F_c)\frac{dR_p}{dt}\Big|_{\text{growth}} + F_c\frac{dR_p}{dt}\Big|_{\text{coarsening}} \tag{11}$$

When $R_{pc} = R_p$, $F_c = 1$; when $R_{pc} \ll R_p$, $F_c = 0$. Similarly, the overall evolution of the precipitate number is described by:

$$\begin{cases} \dfrac{dN}{dt} = F_c\dfrac{dN}{dt}\Big|_{\text{coarsening}} & \text{if} \quad -\dfrac{dN}{dt}\Big|_{\text{coarsening}} > \dfrac{dN}{dt}\Big|_{\text{nucleation}} \\ \dfrac{dN}{dt} = \dfrac{dN}{dt}\Big|_{\text{nucleation}} & \text{if} \quad -\dfrac{dN}{dt}\Big|_{\text{coarsening}} < \dfrac{dN}{dt}\Big|_{\text{nucleation}} \end{cases} \tag{12}$$

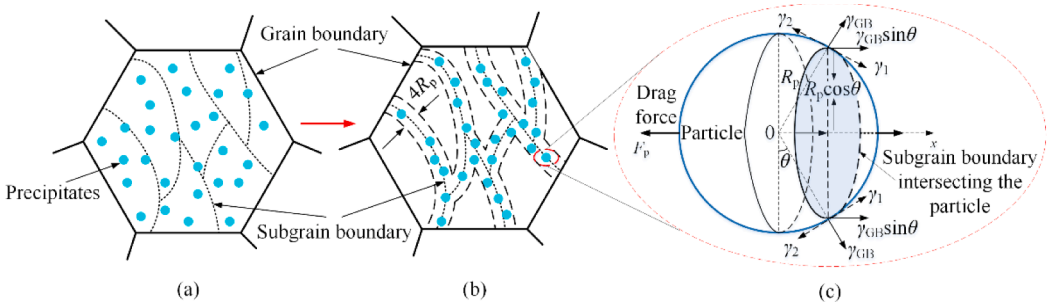

Fig. 3. Schematic view of precipitate distributions (a) at random and (b) at subgrain boundaries. (c) Interaction between a subgrain boundary and a single precipitate.

From mass balance, the instantaneous concentrations of Nb in the matrix can be obtained (Dutta et al., 2001):

$$C_{\mathrm{Nb}} = \left(C_{\mathrm{Nb0}} - \frac{4}{3}\pi R_{\mathrm{p}}^3 N C_{\mathrm{Nb}}^{\mathrm{p}}\right) \Big/ \left(1 - \frac{4}{3}\pi R_{\mathrm{p}}^3 N\right) \tag{13}$$

where C_{Nb0} is the initial concentration of Nb.

2.2.2. Precipitate distribution and average pinning energy on subgrain boundaries

In the model outlined above, the description of precipitate number density N in Eqs. (7) and (10) is based on a random distribution, as schematically shown in Fig. 3(a). However, a more realistic assumption for the precipitate distribution is that the particles lie on (or around) subgrain boundaries in the hot-worked structure (Hansen et al., 1980). Because dislocations mainly concentrate on subgrain boundaries, the formation of precipitates around the subgrain boundaries is energetically favourable, all precipitates are assumed to have centres within a distance R_{p} of the subgrain boundary, i.e. precipitates are distributed with within a range of $4R_{\mathrm{p}}$ on both sides of the subgrain boundary, as shown in Fig. 3(b). The conservation of number of particles requires the number density of precipitates around the subgrain boundaries N_{sg} to satisfy:

$$4\pi R_{\mathrm{g}}^2 \cdot 4R_{\mathrm{p}} \cdot N_{\mathrm{sg}} = 2 \cdot \frac{4}{3}\pi R_{\mathrm{g}}^3 \cdot N \tag{14}$$

where R_{g} is the subgrain radius, $4\pi R_{\mathrm{g}}^2 \cdot 4R_{\mathrm{p}}$ represents the volume of precipitates distributed around the subgrain boundary and the factor 2 accounts for precipitates from adjacent subgrains. Substituting the volume fraction of precipitates $f_{\mathrm{v}} = \frac{4}{3}\pi R_{\mathrm{g}}^3 N$ into Eq. (14), N_{sg} is expressed as:

$$N_{\mathrm{sg}} = \frac{R_{\mathrm{g}}}{8\pi R_{\mathrm{p}}^4} f_{\mathrm{v}} \tag{15}$$

Eq. (15) converts the precipitate number density (calculated under the assumption of a random distribution) to that for precipitation on subgrain boundaries.

The average pinning energy E_{ap} is defined as the average energy to be overcome as a subgrain boundary moves a subunit b on a precipitate particle, when incorporating the interaction between precipitates and subgrain boundaries. It is assumed that the boundary meets the particle at an angle of 90° as Gladman (1966) and Nes et al. (1985) have done, i.e. the boundary intersects the particle across a diametral plane. With this assumption, as shown in Fig. 3(c), the tensions γ_1 and γ_2 of interface between particle and subgrain on both sides of the subgrain boundary cancel each other out, only the surface tension γ_{GB} of the subgrain interface acts on the particle. T T The drag force F_{p} can be calculated as:

$$F_{\mathrm{p}} = 2\pi R_{\mathrm{p}} \cos\theta \cdot \gamma_{\mathrm{GB}} \sin\theta \tag{16}$$

then combining the displacement $\mathrm{d}x = R_{\mathrm{p}}\cos\theta \mathrm{d}\theta$, the total energy to be overcome when the boundary passes the particle can be obtained:

$$Q_{\mathrm{p}} = \int_0^{R_{\mathrm{p}}} F_{\mathrm{p}} \mathrm{d}x = \frac{2}{3}\pi R_{\mathrm{p}}^2 \gamma_{\mathrm{GB}} \tag{17}$$

Following the definition of average pinning energy above,

$$E_{\mathrm{ap}} = \frac{Q_{\mathrm{p}}}{R_{\mathrm{p}}} b = \frac{2}{3}\pi R_{\mathrm{p}} \gamma_{\mathrm{GB}} b \tag{18}$$

This is a novel expression for the energy interaction between on precipitate and subgrain boundaries.

2.3. Post-deformation recrystallization

2.3.1. Post-deformation recrystallization coefficient

During recrystallization at high temperature, the strain-free recrystallized nuclei in certain parts of the deformed region will grow at the expense of consuming the deformed or recovered microstructure; the high angle grain boundaries quickly sweep the high dislocation density area to form a new region with pretty low dislocation density (Humphreys and Hatherly, 2012). The average dislocation density will greatly decrease during this process. The recrystallization coefficient f_{RX} in Eq. (1) quantifies the capability for recrystallized grains to grow and occupy deformed regions. Galindo-Nava and Rivera-Díaz-del-Castillo (2013) have provided an expression for f_{RX} in terms of the ratio between the potential sites for growth and the number of growing grains, $f_{\mathrm{RX}} = (N_{\mathrm{nucl}} - N_{\mathrm{growth}})/N_{\mathrm{growth}}$; where the numerator equals to difference between the total number of subgrains N_{nucl} from whom grain growth occurs and the number of growing grains N_{growth}, accounting for the potential sites for growth; grain growth is a thermally activated process, i.e. $N_{\mathrm{growth}} = N_{\mathrm{nucl}} \exp\left(-\frac{Q_{\mathrm{RX}}}{kT}\right)$. Although this method has successfully described the dynamic softening behaviour caused by dynamic recrystallization during hot deformation in pure FCC metals, alloy steels and low-alloy steels (Galindo-Nava et al., 2014), it cannot be directly applied to post-deformation recrystallization. This is because during hot deformation, the stored strain energy, which is the

driving force for recrystallization, will decrease due to dynamic softening, but the continuous work input from external forces will compensate for the loss of stored energy. Conversely, during annealing the stored strain energy will monotonically decrease, resulting in a depletion of the driving force for recrystallization. Thus, recrystallization rate decays with the progress of static softening. This process is accelerated with an increase in temperature, which in turn increases the grain boundary mobility and promotes grain growth.

Post-deformation recrystallization may be meta-dynamic or static, depending on whether dynamic recrystallization occurs or not during hot deformation. If the strain is less than a critical value triggering dynamic recrystallization, static recrystallization may arise in the subsequent annealing process; otherwise, meta-dynamic recrystallization will take place (Sakai et al., 2014). For meta-dynamic recrystallization, grain growth is triggered post-deformation on freshly recrystallized nuclei; the dynamically recrystallized grains that just nucleated, and that are already present upon the completion of deformation. Thus, in meta-dynamic recrystallization no incubation time is required (Elwazri et al., 2004; Sakai et al., 2014, 1988). It follows that the kinetics of meta-dynamic recrystallization is much faster than that of static recrystallization following deformation, indicating a stronger ability to occupy the deformed regions (Sakai et al., 2014; Tang et al., 2016). However, meta-dynamic recrystallization can still be effectively described by the same form of equation as describing static recrystallization, even though it does not involve an incubation time (Elwazri et al., 2004). Both processes undergo grain growth once recrystallization is initiated as grain grows as a result of interface migration.

Considering all the above, to describe the post-deformation recrystallization, a unified equation is proposed in this work:

$$f_{\mathrm{RX}} = \lambda\left(\frac{\rho}{\rho_0}\right)^{\frac{T_{\mathrm{m}}}{T}}\left(\exp\left(\frac{Q_{\mathrm{RX}}}{kT}\right) - 1\right) \tag{19}$$

where $\lambda \geq 1$ is an acceleration factor for meta-dynamic recrystallization to capture the stronger ability to occupy deformed regions, which value depends on the volume fraction of dynamically recrystallized grains. When dynamic recrystallization has not taken place, the value is set to 1. In the second term, ρ/ρ_0 is used to characterize the effect of the stored energy decay and the power term T_{m}/T is to scale the effect of temperature; T_{m} is the material's melting temperature. The third term in the right hand side represents the ratio between the potential sites for growth and the number of growing grains. It follows the method proposed by Galindo-Nava and Rivera-Díaz-del-Castillo (2013), in which grain growth is treated as a thermally activated process and Q_{RX} is the energy barrier for grain growth.

2.3.2. Energy barrier Q_{RX}

The energy barrier Q_{RX} accounts for the factors promoting and suppressing grain boundary motion. By considering the recrystallized grain to be the result of a dislocation arrangement, the associated energy for grain boundary motion can be approximated by the dissipation energy of dislocations movement on the migrating boundary (Galindo-Nava et al., 2014):

$$E_{\mathrm{disp}} = n_{\mathrm{g}}\frac{\bar{l}}{b}\left[\left(1 + \sum_i x_i^{1/3}\right)\left(1 + \sum_s x_s^{1/3}\right)\right]^{-1} T\Delta S \tag{20}$$

where n_{g} is the number of dislocations comprising the boundaries, x_i and x_s are the atom fraction of the i_{th} interstitial element and the sth substitutional element, respectively. ΔS is the statistical dislocation entropy to account for the thermally-activated dislocation slip paths (Galindo-Nava et al., 2014):

$$\Delta S = k\ln\left(\frac{\dot{\varepsilon}_0 + \vartheta}{\dot{\varepsilon}}\right)^{\left(1+\sum_i x_i^{1/3}\right)\left(1+\sum_s x_s^{1/3}\right)} \tag{21}$$

where $\dot{\varepsilon}_0 = cb\rho$ is the limiting upper value for strain rate, and c is the speed of sound in the material. $\vartheta = \vartheta_{\mathrm{D}}\exp\left(-\frac{E_{\mathrm{m}}}{RT}\right)$ is the migration frequency of vacancy and E_{m} is the vacancy migration energy. Here, ϑ represents the number of atomic sites a vacancy jumps per second and accounts for the interaction of vacancy and dislocation. $\dot{\varepsilon}$ is the strain rate during stress relaxation.

Friedel (1964) and Vohringer (1987) proposed that the internal stress relaxation corresponds to dislocation annihilation and rearrangement, and there is a plastic relaxation strain which can substitute the equivalent elastic strain. Therefore, the corresponding strain rate $\dot{\varepsilon}$ can be related to stress relaxation (decrease rate of the flow stress) by:

$$\frac{\mathrm{d}\sigma}{\mathrm{d}t} = -\dot{\varepsilon}E \tag{22}$$

where E is the Young's modulus. Such relation is consistent with the observation of Hasegawa et al. (1982), obtained by associating the length changes of uniaxially deformed Al single crystals during recovery with the dislocation annihilation and the annealing times. This relationship has been used to establish a recovery model in the study of Verdier et al. (1998) and Tang et al. (2020). From Eq. (2), the rate of decrease in the flow stress can be expressed as:

$$\frac{\mathrm{d}\sigma}{\mathrm{d}t} = \frac{\alpha\mu bM}{2\sqrt{\rho}}\frac{\mathrm{d}\rho}{\mathrm{d}t} \tag{23}$$

Combing Eqs. (22) and (23), and substituting $E = 2(1+\nu)\mu$ (Saxena et al., 2018), the strain rate can be obtained:

$$\dot{\varepsilon} = -\frac{\alpha\mu b M}{4(1+\nu)\sqrt{\rho}}\frac{\mathrm{d}\rho}{\mathrm{d}t} \tag{24}$$

The energy barrier that prevents the grain boundary migration mainly originates from four contributions: the strain of high-angle grain boundaries, the pinning effect of interstitial atoms, the solute drag effect due to substitutional atoms and the pinning due to precipitates.

(1) The strain energy E_{HAGB} of high-angle grain boundaries is proportional to the total strain energy stored in them, $E_{\mathrm{HAGB}} = n_g\frac{\psi}{2}\mu b^2\bar{l}$, where $\psi = 0.6$ is the energy fraction for FCC metals (Galindo-Nava and Rivera-Díaz-del-Castillo, 2013).

(2) Based on the ability of solute elements to hinder the migration of grain boundaries, the solute drag energy of substitutional atoms is estimated from two contributions. One is from the effect of niobium, which has a strong tendency to associate with defects such as vacancies and dislocations more strongly than any other common solute element (Hashmi, 2014). Given that the boundaries move through the vacancy-mediated climb of dislocations (Winning et al., 2010), the drag energy of niobium E_{Nb} estimated from niobium-vacancy interactions is:

$$E_{\mathrm{Nb}} = 2\cdot\frac{\pi n_g\bar{l}}{b}\cdot x_{\mathrm{Nb}}^{1/3}\cdot\left(E_b + E_f\right) \tag{25}$$

where the 2 factor is to account for the boundary encountering niobium atoms on both sides; the second term $\pi n_g\bar{l}/b$ is the total number of potential sites encountering niobium atoms at grain boundaries in which the numerator accounts for the perimeter of a grain; x_{Nb} is the atomic concentration of niobium, $x_{\mathrm{Nb}}^{1/3}$ is the concentration per unit length and accounts for the probability of a boundary encountering a niobium atom; the last term is the energy to escape the effect of a single niobium atom, where E_b is the binding energy of niobium to vacancy and E_f is the vacancy formation energy.

The drag effect of the remaining substitutional atoms on the migrating boundary is weaker and the drag energy E_{sol} can be calculated from (Galindo-Nava et al., 2014):

$$E_{\mathrm{sol}} = -n_g\frac{\bar{l}}{b}\sum_{sol}x_{sol}^{1/3}\Delta G_{\mathrm{sys}} \tag{26}$$

where $\sum_{\mathrm{sol}}x_{\mathrm{sol}}$ accounts for the total atom concentration of the remaining solute and ΔG_{sys} is the free energy of the mixture.

(3) The energy to be overcome due to interstitial atoms impeding grain boundary motion is estimated by the subgrain boundary energy γ_{GB} around the potential sites for carbon segregation at boundaries (Galindo-Nava et al., 2014):

$$E_{\mathrm{inter}} = 2\pi n_g\gamma_{GB}x_C^{1/3}\bar{l}b \tag{27}$$

where x_C is the atomic concentration of carbon. Here, only the effect of carbon is considered, it should be replaced by the total interstitial atom concentration $\sum_i x_i$ if other elements are included, such as boron.

(4) The pinning energy from precipitates E_p is equal to the average pinning energy of a single precipitate E_{ap} (Eq. (18)) multiplied by the number of precipitates on the boundaries:

$$E_p = 2N_{sg}^{1/3}\cdot\pi n_g\bar{l}\cdot E_{\mathrm{ap}} = \left(\frac{4\pi}{3}\right)^{\frac{2}{3}}\pi n_g b\bar{l}\gamma_{GB}\left(\frac{R_g f_v}{6R_p}\right)^{\frac{1}{3}} \tag{28}$$

where $N_{sg}^{1/3}$ (obtained from Eq. (15)) is the number of precipitates per unit length around the boundary and accounts for the probability of precipitates on the boundary, the factor 2 is to account for the boundary encountering precipitates on both sides.

Incorporating all the factors for the energy barrier, Q_{RX} calculated from

$$Q_{\mathrm{RX}} = S_{\mathrm{sub}}\left(E_{\mathrm{disp}} - E_{\mathrm{HAGB}} - E_{\mathrm{Nb}} - E_{\mathrm{sol}} - E_{\mathrm{inter}} - E_p\right) \tag{29}$$

where $S_{\mathrm{sub}} = 6b/(n_g k_c\bar{l})$ accounts for the available sites for grain nucleation on pre-existing subgrains per dislocation and $k_c = \frac{12\pi(1-\nu)}{2+\nu}\left(1+\frac{T\Delta S}{\mu b^3/2}\right)$ (Galindo-Nava et al., 2014). Substituting Eqs. (20) - (28), the energy barrier Q_{RX} is derived as:

$$Q_{\mathrm{RX}} = \frac{6}{k_c}\left(kT\ln\left(\frac{\dot{\varepsilon}_0+\vartheta}{\dot{\varepsilon}}\right) - 0.3\mu b^3 - 2\pi x_{\mathrm{Nb}}^{1/3}\left(E_b+E_f\right) + \sum_{sol}x_{sol}^{1/3}\Delta G_{\mathrm{sys}}\right.$$
$$\left. -2\pi b^2 x_C^{1/3}\gamma_{\mathrm{GB}} - \left(\frac{4\pi}{3}\right)^{\frac{2}{3}}\pi b^2\gamma_{\mathrm{GB}}\left(\frac{R_g f_v}{6R_p}\right)^{\frac{1}{3}}\right) \tag{30}$$

Both static and meta-dynamic recrystallization can be described by the same formulation, as the associated grain growth process is

equal, only differing by the presence of an incubation time (Elwazri et al., 2004). Thus, Q_{RX} for grain growth does not depend on whether it is static or meta-dynamic recrystallization, but the calculated results of energy barrier for both are different because the deformation state variables are different in the calculation. Incorporating Eq. (30) into Eq. (19), the post-deformation coefficient can be calculated by:

$$f_{RX}=\lambda\left(\frac{\rho}{\rho_0}\right)^{\frac{\tau_m}{T}}\left(\exp\left(\frac{6}{k_c kT}\left(kT\ln\left(\frac{\dot{\varepsilon}_0+\vartheta}{\dot{\varepsilon}}\right)-0.3\mu b^3-2\pi x_{Nb}^{1/3}\left(E_b+E_f\right)\right.\right.\right.$$
$$\left.\left.\left.+\sum_{sol}x_{sol}^{1/3}\Delta G_{sys}-2\pi b^2 x_C^{1/3}\gamma_{GB}-\left(\frac{4\pi}{3}\right)^{\frac{2}{3}}\pi b^2\gamma_{GB}\left(\frac{R_g f_v}{6R_p}\right)^{\frac{1}{3}}\right)\right)-1\right) \tag{31}$$

If $f_{RX}\le 0$ the recrystallization is energetically unfavourable, then the f_{RX} is set to 0.

2.4. Incubation time for static recrystallization

If the process of post-deformation recrystallization is static recrystallization (dynamic recrystallization is not initiated during deformation), it is necessary to determine the incubation time during annealing. Considering grain nucleation from subgrains (Humphreys, 1997; Hurley and Humphreys, 2003), they should display a critical size before becoming a recrystallized nucleus. Thus, an incubation time is required for subgrains to grow to a critical size (Zurob et al., 2006), as formulated next.

2.4.1. Critical subgrain size

During annealing, dislocations rearrange by recovery; once high angle boundaries form by the accumulation of dislocations in the boundaries, the subgrain may become a nucleus to initiate recrystallization (Humphreys and Hatherly, 2012). From the point of view of energy balance, to initiate recrystallization the total stored energy at the boundaries should be equal to the addition of (Galindo-Nava and Rivera-Díaz-del-Castillo, 2013): (1) the strain energy to nucleate the dislocation-free grain $E_{grain}=n_g\frac{\mu b^2}{2\bar{l}}(b\bar{x}_{grain})$, (2) the displacement energy for boundary-dislocation to initiate grain growth E_{disp} (Eq. (20)), and (3) the equivalent slip energy for dislocation migration from the subgrain interior to the boundaries $E_{int}=n_{int}\frac{\bar{l}}{b}[(1+\sum_i x_i^{1/3})(1+\sum_s x_s^{1/3})]^{-1}T\Delta S$. Due to the presence of solute atoms and precipitates, the total stored energy is comprised of the stored energy of dislocation at boundaries $E_{sub}=n_g\frac{1}{2}\mu b^2\bar{l}$, the solute-drag energy E_{Nb} (Eq. (25)) and E_{sol} (Eq. (26)), the impeding energy from interstitial atoms E_{inter} (Eq. (27)) and the pinning energy from precipitates E_p (Eq. (28)). Therefore, the energy balance can be expressed as:

$$E_{sub}+E_{Nb}+E_{sol}+9E_{inter}+E_p=E_{grain}+E_{disp}+E_{int} \tag{32}$$

where the factor 9 accounts for the number of directions for interstitial atoms interacting with the subgrain boundaries (Galindo-Nava et al., 2014); $\bar{x}_{grain}$ in E_{grain} accounts for the boundary length of the cross-section of an incipient grain; $n_{int}=n_g/k_c$ in E_{int} is the number of dislocations in subgrain interiors (Galindo-Nava and Rivera-Díaz-del-Castillo, 2013). Substituting corresponding expressions into Eq. (32), the critical subgrain size to start recrystallization R_c is derived as:

$$R_c=\frac{\bar{x}_{grain}}{2\pi}=\frac{1}{2\pi b\rho}\left(1+\frac{4\pi x_{Nb}^{1/3}\left(E_b+E_f\right)}{\mu b^3}-\frac{2\sum_{sol}x_{sol}^{1/3}\Delta G_{sys}}{\mu b^3}+\frac{36\pi\gamma_{GB}x_C^{1/3}}{\mu b}\right.$$
$$\left.+\left(\frac{4\pi}{3}\right)^{\frac{2}{3}}\frac{2\pi\gamma_{GB}}{\mu b}\left(\frac{R_g f_v}{6R_p}\right)^{\frac{1}{3}}-2\left(1+\frac{1}{k_c}\right)\frac{kT}{\mu b^3}\ln\left(\frac{\dot{\varepsilon}_0+\vartheta}{\dot{\varepsilon}}\right)\right) \tag{33}$$

2.4.2. Incubation time

The growth rate of average subgrain size is determined by (Humphreys and Hatherly, 2012):

$$\frac{dR_g}{dt}=P_{sb}M_{sb} \tag{34}$$

When precipitation takes place, P_{sb} represents the net driving force for subgrain growth and can be calculated by (Humphreys and Hatherly, 2012; Momeni et al., 2014):

$$P_{sb}=\frac{2\gamma_{GB}}{R_g}-\frac{3\gamma f_v}{2R_p} \tag{35}$$

M_{sb} is the mobility of subgrain boundaries and can be expressed as (Humphreys and Hatherly, 2012):

$$M_{sb}=\frac{m_0}{T}\exp\left(-\frac{Q_m}{RT}\right) \tag{36}$$

where m_0 is a material constant, Q_m is the activation energy of subgrain boundary mobility.

By integrating Eq. (34), the average size of subgrain at time t is obtained as:

$$R_g = R_{g0} + \int_0^t P_{sb} M_{sb} \mathrm{d}t \tag{37}$$

where R_{g0} is the initial average subgrain size. Considering a Rayleigh distribution of subgrains, the largest subgrain size R_{gmax} is approximately $2.5R_g$ (Zurob et al., 2006). Based on the basic idea of nucleation criterion mentioned before, i.e. $R_{gmax} = R_c$, the incubation time t_c can be obtained by solving the following equation:

$$2.5\left(R_{g0} + \int_0^{t_c} P_{sb} M_{sb} \mathrm{d}t\right) = R_c(t_c) \tag{38}$$

If the largest subgrain size is always smaller than the critical subgrain size, i.e. Eq. (38) has no solution, it indicates recrystallization will not occur within the given annealing time.

Due to the complex simultaneous processes accounted for in this model, a flow chart is show shown in Fig. 4 to outline the sequence of calculations undertaken in this approach. The presence of static or meta-dynamic recrystallization in Fig. 4 depends on whether dynamic recrystallization was previously triggered during the deformation process (Uranga et al., 2003). As for Nb-free steels, in the calculation initialization step shown in Fig. 4, when Nb is absent, the precipitation calculation is not performed.

3. Model validation

3.1. Model parameters

Successful coupling of the complex softening physical processes after deformation (Fig. 2) can be confirmed through a series of stress relaxation experiments. In such experiments, specimens will be compressed first at a given strain, strain rate and temperature, with the stroke being fixed after deformation and the stress at different moments recorded to obtain the stress relaxation curves. The model presented here is tested against 37 stress relaxation curves obtained from experiments (Bäcke, 2010; Engberg and Lissel, 2008; Miao et al., 2010; Zhang et al., 2008). These experimental curves feature 6 microalloys under a wide range of deformation conditions. Table 1 shows the corresponding chemical composition of each steel.

The physical parameters input to the model are shown in Table 2. Except for the stress intensity factor $\xi = 32$ and the constant of subgrain boundary mobility $m_0 = 1.02 \times 10^7$, which were fitted to our dataset of experimental results within reasonable ranges

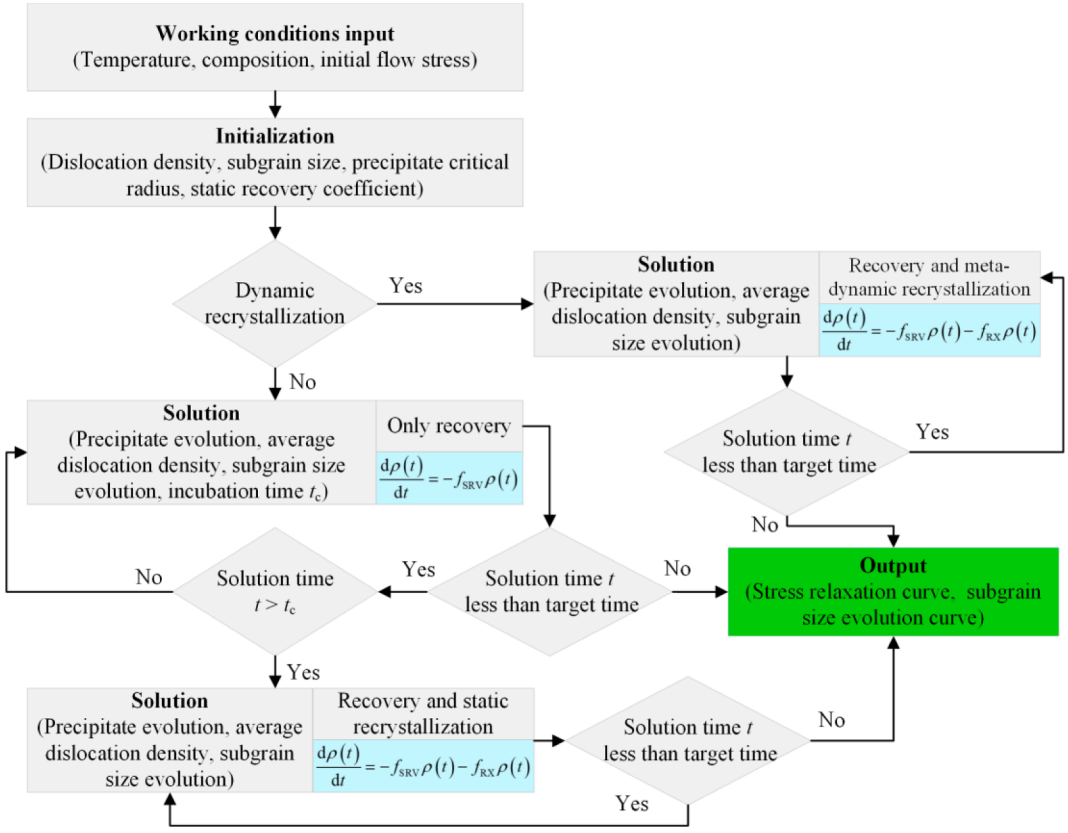

Fig. 4. Model calculation flow chart.

Table 1
Composition of experimental steel (wt.%).

Steel	C	Mn	Si	Al	Nb	Ti	V	N	Reference
1#	0.200	1.200	0.400	0.030	–	–	–	–	(Zhang et al., 2008)
2#	0.200	1.200	0.400	0.030	0.030	–	–	–	(Zhang et al., 2008)
3#	0.064	0.648	0.007	0.041	0.002	0.001	0.004	0.006	(Engberg and Lissel, 2008)
4#	0.065	1.085	0.007	0.055	0.034	0.001	0.006	0.004	(Bäcke, 2010)
5#	0.066	1.323	0.036	0.040	0.055	0.001	0.005	0.005	(Bäcke, 2010)
6#	0.040	1.750	0.220	0.030	0.100	0.015	–	0.004	(Miao et al., 2010)

according to the literature (Humphreys and Hatherly, 2012; Nes, 1997), all physical parameters used in the present model were adopted from literature or computed using thermochemical software. The recovery activation energy is expected to be between 0.6 and 1 times the self-diffusion energy of pure γ-iron (Nes, 1995; Zurob et al., 2002); here a value of $U_{SRV} = 0.8Q_{Fe}$ is chosen. The magnitude of the Burgers vector b, the lattice spacing a, the radius of the dislocation core R_{core} and the proportionality constant F depend on the type of crystal structure. Widely used values are listed in Table 2 for FCC. As studied by Xu (1997), the binding energy of niobium to vacancy E_b is in the range of 0.15 to 0.60 eV, and the common value of 0.45 eV for Nb microalloyed steel (Wang et al., 2018) is adopted in the present study. ΔG_{sys} values for low-alloy steels were fitted to a formula to describe the temperature variation based on calculations from Thermocalc by Galindo-Nava et al. (2014) and for the tested composition ranges the values did not vary significantly with composition (less than -2 kJ•mol^{-1}). Since the compositions of tested steels in this work are within their tested range, the same equation was employed for all cases. The remaining parameters in Table 2, such as the vacancy formation energy E_f, the migration energy E_m, the self-diffusion energy of pure γ-iron Q_{Fe}, the bulk diffusion D_{bulk} and the pipe diffusion coefficients D_{pipe}, all come from established literature (Allen and Was, 1998; Dutta et al., 2001; Galindo-Nava et al., 2014; Geise and Herzig, 1985; Momeni et al., 2014; Vasilyev et al., 2011; Zurob, 2003; Zurob et al., 2002) and have been used in many other studies.

According to the observation of Winning et al. (2001), the activation energy of low angle grain boundary mobility is very close to the self-diffusion activation energy. Here it is assumed that the activation energy of subgrain boundary mobility, Q_m, equals the self-diffusion activation energy of austenite. The drag effect of Nb on subgrain boundary mobility is captured through the effect of Nb on self-diffusion activation energy and an empirical formula $Q_m = Q_{Fe} + 132,594(100x_{Nb})^{0.263}$ derived by Vasilyev et al. (2011) from experiments is used to evaluate Q_m with different contents of Nb.

Based on calculations from ThermoCalc software (version 2019b with TCFE9 database) (Andersson et al., 2002), there are no vanadium precipitates present in the austenite temperature region for the steels listed in Table 1. Furthermore, the equilibrium concentration of Ti at 1523 K is only 0.004% for steel 6#, indicating that TiN hardly dissolves before deformation. With this in mind, the precipitation process of TiN during stress relaxation will not be considered in steel 3#, 4# and 5# owing to the small Ti concentration. Instead, the effect of TiN particles on softening behaviour depends on their size and volume fraction before stress relaxation. The volume fraction is obtained by mass balance similar to Eq. (13). The measurements of Zhang et al. (2018) on a steel similar to 6# show that the size of TiN particles after reheating is between 30 and 100 nm. Therefore, an average size of 65 nm is set as for TiN particles. In addition, the solubility product of NbC from the calculation of ThermoCalc is fitted by the expression $\log_{10}K_s = A - B/T$ for steel 2# and 4# to 6#, and the fitting constants A and B are shown in Table 3.

3.2. Comparison with experimental data

The stress evolution can be calculated from Eq. (2) by substituting into the average dislocation density extracted from Eq. (1). The initial average dislocation density ρ_0 is estimated by Eq. (2) based on the initial stress $\sigma(t = 0)$ and the steady-state stress σ_0 obtained from the experimental results. Furthermore, the meta-dynamic recrystallization acceleration factor λ is set to 3 for all test conditions

Table 2
Physical parameters employed in the model.

Symbol	Value	Reference
b (nm)	0.258	(Frost and Ashby, 1982)
a (nm)	0.445	(Dutta et al., 2001)
R_{core} (nm)	0.5	(Dutta et al., 2001)
E_b (eV)	0.45	(Wang et al., 2018)
E_f (eV)	1.4	(Allen and Was, 1998)
Q_{Fe} (kJ/mol)	312	(Vasilyev et al., 2011)
E_m (eV)	1.28	(Galindo-Nava et al., 2014)
D_{pipe} (m^2/s)	$4 \times 10^{-4}\exp(-172{,}500/RT)$	(Zurob et al., 2002)
D_{bulk} (m^2/s)	$8.3 \times 10^{-5}\exp(-266{,}500/RT)$	(Geise and Herzig, 1985)
F	0.0075	(Zurob, 2003)
μ (MPa)	85,335–34T	(Galindo-Nava et al., 2014)
γ (J/m^2)	0.5	(Dutta et al., 2001)
γ_{GB} (J/m^2)	0.32	(Momeni et al., 2014)
ΔG_{sys} (kJ/mol)	16–0.045T-1.4 $\times 10^{-5}T^2$	(Galindo-Nava et al., 2014)

Table 3
Solubility product of NbC.

Constant	2#	4#	5#	6#
A	0.848	−0.828	0.341	0.703
B	9509.358	7585.523	9191.723	9555.107

with the partial dynamic recrystallization. The initial subgrain size is estimated from the initial average dislocation density by the method developed by Galindo-Nava and Rivera-Díaz-del-Castillo (2012).

Steels 1# and 2# have the same composition except that 1# does not contain Nb. Fig. 5(a) and (b) show a comparison between the model and the corresponding experimental results at different temperatures for both steels. For all conditions, the strain and strain rate are 0.22 and 1 s^{-1}, respectively, before stress relaxation. Following Zhang et al. (2008), partial dynamic recrystallization takes place in steel 1# at temperatures above 1273 K and in steel 2# above 1323 K, indicating that post-deformation recrystallization in these conditions is meta-dynamic. Whether it is steel 1# without Nb or steel 2# with Nb, the model shows good agreement with experimental results, except for steel 2# at 1173 K, where the experiment shows a moderately slower softening rate. The model predicts that the static recrystallization of steel 1# hardly needs an incubation time for temperatures above 1173 K. However, for steel 2# containing Nb, the incubation times are at a range from 0.11 to 7 s for temperatures from 1173 to 1273 K.

A sharp inflection point in some stress relaxation curves can be found in Fig. 5(b) (e.g. at 1173 K). This stems from the abrupt average dislocation density reduction caused by recrystallization exceeding that of recovery only, as shown in Fig. 5(c). Furthermore, with a lower driving force and a longer incubation time, the inflection point is more obvious. Because of the incubation time increases, the recovery rate continues to decrease, which causes a greater gap in the decreasing rate of dislocation density between recovery and recrystallization causing a more marked inflection point. Fig. 5(d) presents the evolution of the volume fraction, average and critical radius for precipitates corresponding to the condition in Fig. 5(b) for steel 2#, which shows that the volume fraction increases faster with temperature decrease while the precipitate growth rate decreases with it. At 1223 K, the volume fraction is almost close to the equilibrium concentration about 90 s after deformation, and the average radius is close to the critical radius at about 120 s, which indicates that the precipitate begins to coarsen. However, at 1323 K, the volume fraction is almost zero, although the average radius

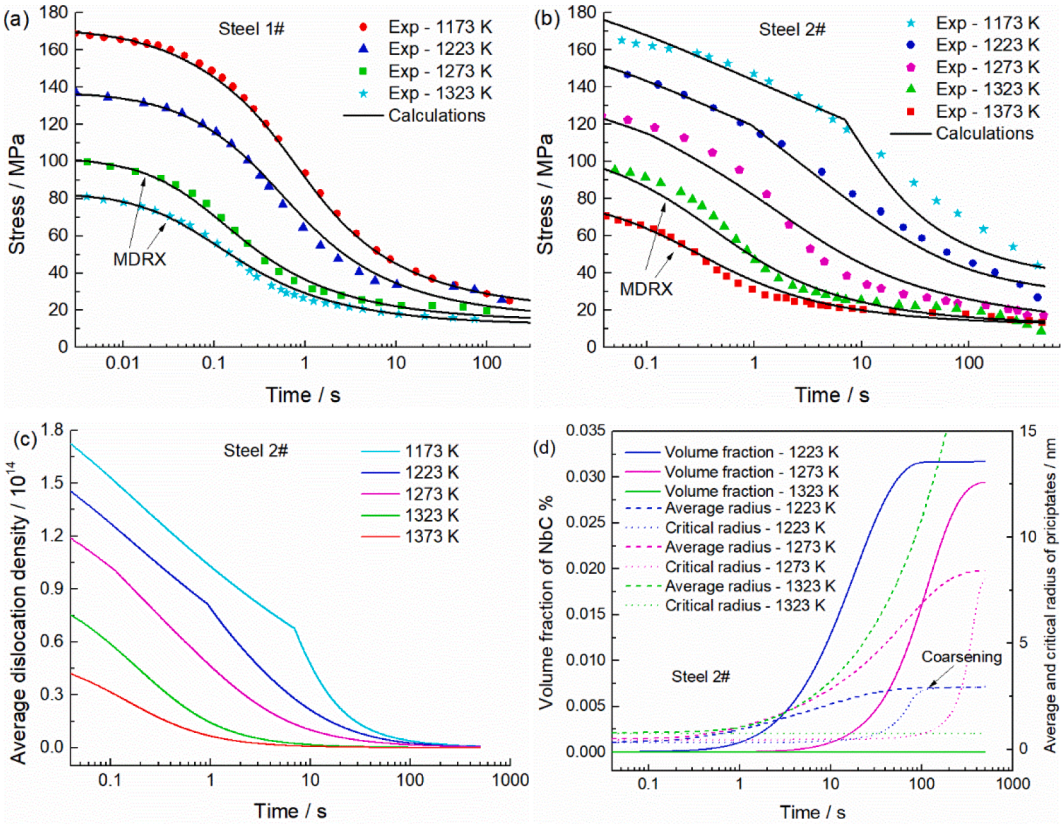

Fig. 5. Stress relaxation curve for (a) steel 1# and (b) steel 2# at different temperatures; the strain and strain rate are 0.22 and 1 s^{-1} for all samples, respectively, before stress relaxation (Zhang et al., 2008); (c) shows the evolution of the average dislocation density corresponding to the condition in (b) for steel 2#, and the corresponding evolution of the volume fraction, average and critical radius for precipitates is presented in (d). MDRX: meta-dynamic recrystallization.

has a faster growth rate compared to that at 1223 and 1273 K. The reason behind this is the driving force of precipitation decreases rapidly with temperature increase, which makes it impossible to form a large number of precipitates in a short period of time. At 1273 K, although the volume fraction is not close to the equilibrium concentration within the experimental time (600 s), it still has a high level; the coarsening will occur over a longer time.

The model results and comparison to experiment for steel 3# at different strain rates and temperatures are shown in Fig. 6, where a strain of 0.4 was applied before stress relaxation for all working conditions. With a strain of 0.4, the stress-strain curves given in literature (Engberg and Lissel, 2008) show that partial dynamic recrystallization is present above 1273 K at a strain rate of 1 s^{-1}, but the dynamic recrystallization is complete at a strain rate of 0.1 s^{-1} for the same temperature range. As shown in Fig. 6(a) and (b), all model results agree well with experimental results at strain rates of 0.1 s^{-1} and 1 s^{-1} for different temperatures, except for 1123 K, where the model shows a higher softening rate. Based on calculations by ThermoCalc, the phase transition temperature (T_{Ar3}) is 1140 K for steel 3#. Therefore, the discrepancy between modelling and experiment can be due to the transition from austenite into ferrite at 1123 K, and this effect is more noticeable at a strain rate of 0.1 s^{-1} as the longer deformation time causes a larger volume fraction of ferrite.

Fig. 7(a) shows the results for steel 3# and 4# at the same working conditions. The post-deformation recrystallization is meta-dynamic for steel 3#, while that is static recrystallization for steel 4# which has a higher content of Nb. Furthermore, Fig. 7(b) – (f) show the results for steel 4# and 5# at different temperatures, strains and strain rates. It should be mentioned that the abrupt fluctuations in stress near 0.2 s for experiment are a machine artefact (Karjalainen et al., 1997), they are also found in Fig. 6 but are less noticeable. Ignoring these fluctuations, all results in Fig. 7 show a remarkable agreement for very wide temperature ranges at different compositions, strains and strain rates.

Fig. 8(a) shows the model results for high Nb steel 6# at different temperatures with a strain of 0.29 and strain rate of 1 s^{-1}. Recrystallization does not occur after deformation below 1273 K due to the strong pining effect of precipitates and the strong drag of Nb atoms. As shown in Fig. 8(b), the maximum subgrain size does not exceed the critical subgrain size during the stress relaxation at the temperature 1173 K and 1273 K. However, for temperature 1323 K, due to the decrease in precipitation driving force, the pinning effect of precipitation is significantly weakened, which makes the maximum subgrain size overtake the critical subgrain size at 0.95 s, promoting static recrystallization. At 1373 K, dynamic recrystallization is triggered during deformation and meta-dynamic recrystallization occurs in the subsequent stress relaxation. Furthermore, Miao et al. (2010) observed the microstructure evolution of steel 6# during the stress relaxation process described above and the microstructure at 3, 60 and 240 s after deformation at 1273 K are shown in Fig. 9(a) – (c). No obvious recrystallized structure can be found, indicating static recrystallization did not occur, consistent with the prediction of the model. Since recrystallization nucleation is not taking place during the stress relaxation process, the microstructure evolution can be regarded as the growth of subgrains to form a new grain structure. It is similar to continuous recrystallization as described by Humphreys and Hatherly (2012). Therefore, in this case, the subgrain size can be approximately estimated by the grain structure which is distinguished by the grain boundary and its orientation (Cahn and Haasen, 1983). Fig. 9(d) shows the subgrain size evolution calculated from the model and their comparison with the statistics obtained from experiments at different times (3, 60, 240 s). The maximum and minimum values have a good agreement, but the average subgrain size from the model is slightly larger than experiments. This can be attributed to neglecting the influence of boundary orientation changes during annealing. As shown by the experimental results obtained by Winning et al. (2001), low-angle boundaries move more rapidly than their high-angle counterparts at high temperatures. Therefore, as the recovery progresses, the average mobility of boundaries will decrease as some of the low angle boundaries become high angle boundaries. This causes the actual grain structure size to be smaller than the subgrain size calculated by the mobility of low-angle boundaries.

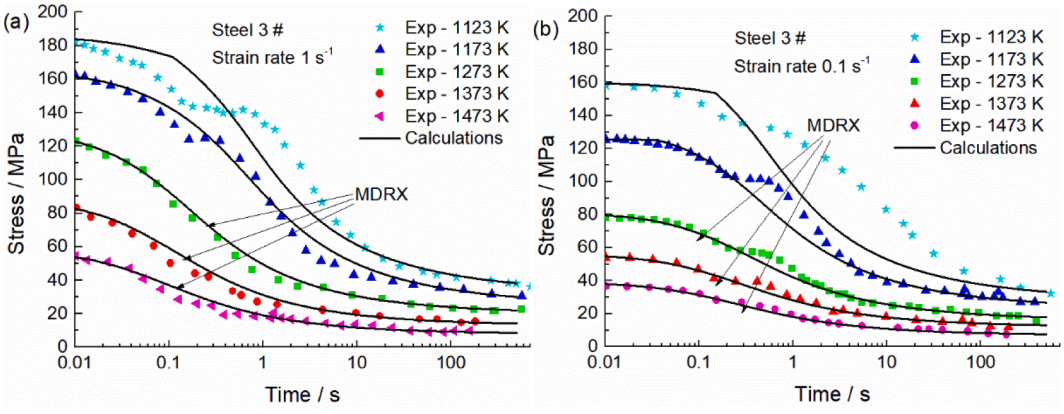

Fig. 6. Stress relaxation curve for steel 3# at strain 0.4 and strain rate (a) 1 s^{-1} and (b) 0.1 s^{-1} (Engberg and Lissel, 2008).

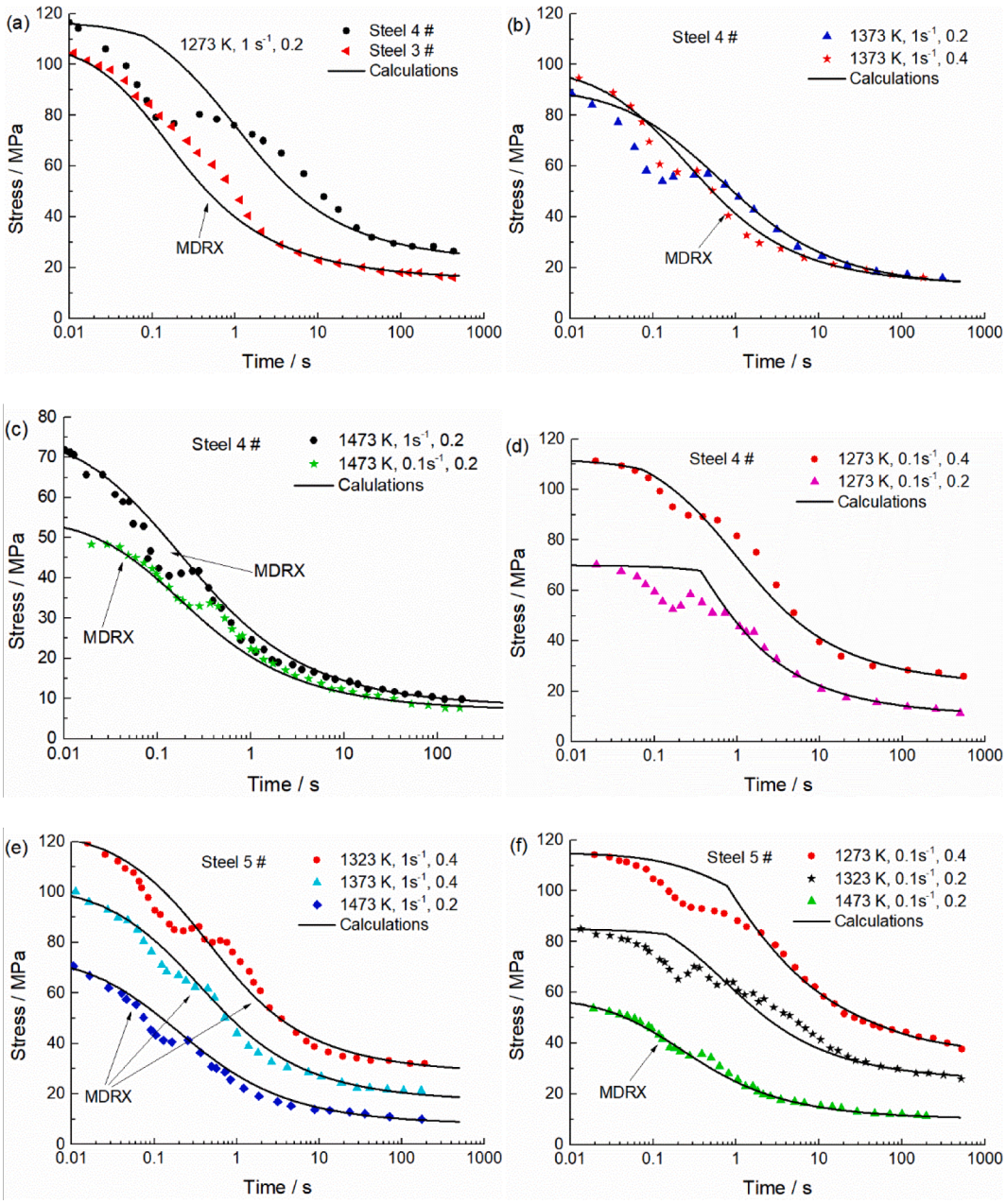

Fig. 7. Stress relaxation curve for (a) steel 3# and 4# at the same working condition; (b), (c), (d) steel 4#, (e), (f) steel 5# at different deformation conditions and annealing temperature; the corresponding temperature, strain rate and strain are shown in the legend (Bäcke, 2010; Engberg and Lissel, 2008). Dots represent the experimental data.

4. Discussion

4.1. Multiple physical processes

A novel approach has been developed based on the thermostatistical plasticity theory to describe stress relaxation after hot deformation. In this method, five physical metallurgical phenomena are incorporated: recovery, static recrystallization, meta-dynamic recrystallization, solute drag and precipitation; they are all coupled using a unified differential equation (Eq. (1)) to capture the evolution of the average dislocation density. The model has been applied to microalloyed steels to describe the stress relaxation process with very good accuracy. More specifically, the model incorporates the following processes:

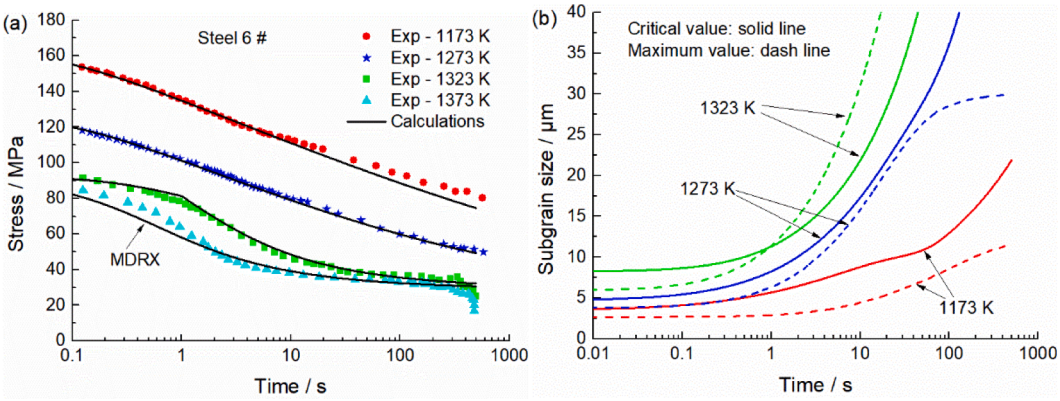

Fig. 8. Stress relaxation curve for the (a) steel 6# at different temperatures. The true strain is 0.29 and strain rate is 1 s^{-1} (Miao et al., 2010). (b) shows the evolution of critical and maximum subgrain size at different temperature for steel 6#.

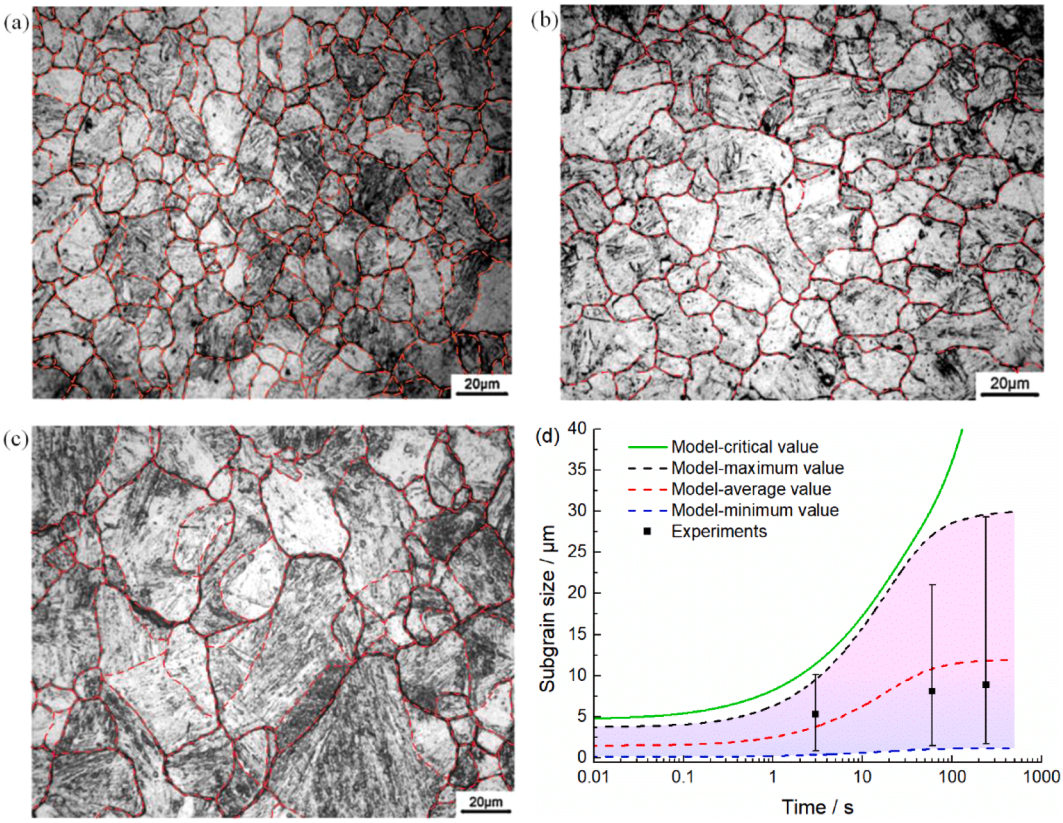

Fig. 9. Microstructure of steel 6# under 29% strain and holding for (a) 3 s, (b) 60 s and (c) 240 s (Miao et al., 2010); (d) shows the corresponding subgrain size and the model results. Dotted red boundary lines represent subgain boundaries.

(1) Description of recovery and both static or meta-dynamic recrystallization.
(2) Evolution of the number density and volume fraction for precipitates.
(3) The critical subgrain size and incubation time for static recrystallization.
(4) Effect of solute drag and precipitation on the incubation time and softening rate.
(5) The subgrain size evolution and distribution.
(6) The temperature, deformation state, and composition dependence of all the above.

Prior to this, few models could simultaneously combine these factors to describe the stress relaxation process. In the present model,

the evolution of the average dislocation density is directly obtained by solving the unified differential equation (Eq. (1)). In contrast with this, previous methods (Bäcke, 2010; Engberg and Lissel, 2008; Zurob et al., 2002) first divided the material into recrystallized and non-recrystallized regions, and the dislocation density evolution of the non-recrystallized regions and the volume fraction of recrystallization were calculated separately. Then, with a given dislocation density for recrystallized regions, the average dislocation density of the alloy is estimated by a mixture of the dislocation density in the non-recrystallized and recrystallized regions.

In contrast with such approaches, the softening effect of recrystallization is not described here by the evolution of the recrystallization volume fraction. Instead, the post-deformation recrystallization coefficient f_{RX} (Eq. (31)) is used to incorporate the effects of recrystallization on softening behaviour and it can capture both static and meta-dynamic recrystallization in a simple way. Dislocation entropy is incorporated into the model to estimate the energy dissipation during grain boundary motion, and the effects of solute drag and precipitation are introduced through the calculation of an energy barrier Q_{RX} for grain growth. Since a detailed description of recrystallization is not incorporated in the calculation, some common fitting parameters such as grain boundary mobility and energy can be circumvented, which makes the model more adaptable. However, this also misses the information on the recrystallized grain size.

The calculation of incubation time for static recrystallization is inspired by the treatment by Zurob et al. (2006), but the expression for the critical subgrain size R_c (Eq. (33)) is derived based on the energy balance introduced here for the first time. This balance describes the competition between the deformation stored energy and the energy required to trigger static recrystallization. Prior to this work, almost all related studies adopted the classical form $R_c = \gamma/\Delta G$ (Humphreys and Hatherly, 2012; Min et al., 2020), which was first derived by Bailey and Hirsch (1962), to calculate critical subgrain size. If substituting the expression of stored energy $\Delta G = 0.5\mu b^2\rho$ (Humphreys and Hatherly, 2012; Li et al., 2009) into the classical form, it can be found that the critical subgrain size only depends on the grain boundary energy γ except for the average dislocation density, which indicates that a very accurate grain boundary energy is required to evaluate the critical subgrain size, which is hard to find and often needs to be fitted. Moreover, the grain boundary energy is not constant during annealing (Humphreys and Hatherly, 2012). This restricts the calculation accuracy and applicability of classical formulations. It is worth noting both classical approaches and Eq. (33) indicate that the critical subgrain size is inversely proportional to the average dislocation density. However, the present approach incorporates the effects of the solute atoms, precipitates and average dislocation density on the critical subgrain size can be clearly described in Eq. (33), making such calculation more robust and adaptable.

4.2. Texture and grain size evolution

The present approach captures the overall transformation kinetics adopting a thermostatistical approach. As such, although the capability for recrystallized grains to grow and occupy the deformed regions is predicted, details on grain growth size are missed and many studies (Aashranth et al., 2017, 2018; Bozzolo et al., 2013; Zouari et al., 2014) have indicated that deformation during/after grain growth is important for subsequent deformation, so it shall be considered in future work. Moreover, it fails to incorporate detailed microstructural information required to describe plastic deformation in three-dimensional structures. These include, for instance, hot rolled bar with a well-defined grain orientation, or additively manufactured components where a concentrated heat source leads to strong texture and mechanical properties anisotropy. It is now known that in additive manufacturing techniques, such as laser powder bed fusion, dynamic recrystallization and recovery can take place (Heidarzadeh et al., 2021; Sabzi et al., 2020, 2021). The present approach would thus fail in providing such spatial information, but would be first to supply a method to describe softening upon building, essential to control residual stresses.

The method provided here can readily be applied to additive manufacturing. For instance, in laser powder bed fusion, once the laser beam leaves the melt pool a contraction follows rapid solidification. This produces a strain rate that, rather than being described by Eq. (24), depends directly on the thermal gradients and process parameters such as hatch distance and layer thickness (Sabzi et al., 2020, 2021). Given that this method allows the calculation of the dynamic recovery and recrystallization, the total strain (the sum of thermal and residual strains) can be calculated.

5. Conclusions

A model is proposed to describe the overall dislocation density evolution after hot deformation. The approach is the first in simultaneously accounting for softening processes including recovery and recrystallization (both static and meta-dynamic). The softening processes are described adopting a thermostatistical approach, which uniquely incorporates the effects of alloy composition, temperature and relaxation rate.

Precipitation, accounting for the overall transformation kinetics (nucleation, growth and coarsening) is considered. Precipitate nucleation is considered at subgrain boundaries, so subgrain evolution is tracked throughout the stress relaxation process. Subgrain growth is shown to agree with experimental results. The interaction of precipitates with the recrystallization process is quantified by the model.

Solute drag, both substitutional and interstitial, is accounted for in recrystallization kinetics. The precipitation kinetics thus links with softening as mass balance restricts the solute concentration in the matrix.

Overall, the model precisely describes softening in 37 stress relaxation conditions for six alloy grades. The strategy outlined here can readily be adopted in other alloy families, and other technologies where stress relaxation is of great importance such as additive manufacturing.

CRediT authorship contribution statement

Jianwei Zhao: Conceptualization, Methodology, Writing – original draft. **Quan Yang:** Funding acquisition, Supervision. **Hossein Eskandari Sabzi:** Formal analysis, Methodology. **Wei Wen:** Formal analysis, Methodology. **Pedro E.J. Rivera-Díaz-del-Castillo:** Project administration, Funding acquisition, Writing – review & editing, Supervision, Conceptualization.

Declaration of Competing Interest

The authors declare that they have no known competing financial interests or personal relationships that could have appeared to influence the work reported in this paper.

Acknowledgements

This work was supported by the China Postdoctoral Science Foundation, under Grant no. 2021M690352. PEJRDDC is grateful to the Engineering and Physical Sciences Research Council U.K. for the provision of funding via grant EP/L025213/1 (Designing Alloys for Resource Efficiency), and to the Royal Academy of Engineering for funding his Chair.

References

Aashranth, B., Davinci, M.A., Samantaray, D., Borah, U., Albert, S.K., 2017. A new critical point on the stress-strain curve: delineation of dynamic recrystallization from grain growth. Mater. Des. 116, 495–503.
Aashranth, B., Samantaray, D., Davinci, M.A., Murugesan, S., Borah, U., Albert, S.K., Bhaduri, A., 2018. A micro-mechanism to explain the post-DRX grain growth at temperatures>0.8 Tm. Mater. Charact. 136, 100–110.
Allen, T., Was, G., 1998. Modeling radiation-induced segregation in austenitic Fe–Cr–Ni alloys. Acta Mater. 46, 3679–3691.
Andersson, J.-.O., Helander, T., Höglund, L., Shi, P., Sundman, B., 2002. Thermo-Calc & DICTRA, computational tools for materials science. Calphad 26, 273–312.
Argon, A.S., Moffatt, W., 1981. Climb of extended edge dislocations. Acta Metall. 29, 293–299.
Bäcke, L., 2010. Modeling the effect of solute drag on recovery and recrystallization during hot deformation of Nb microalloyed steels. ISIJ Int. 50, 239–247.
Bailey, D., Flanagan, W., 1967. The relationship between dislocation density and flow stress in materials deforming by a peierls-nabarro mechanism. Philos. Mag. 15, 43–49.
Bailey, J., Hirsch, P.B., 1962. The recrystallization process in some polycrystalline metals. Proc. R. Soc. London, Ser. A 267, 11–30.
Bammann, D., Solanki, K., 2010. On kinematic, thermodynamic, and kinetic coupling of a damage theory for polycrystalline material. Int. J. Plast. 26, 775–793.
Bozzolo, N., Agnoli, A., Souai, N., Bernacki, M., Logé, R.E., 2013. Strain induced abnormal grain growth in nickel base superalloys. Mater. Sci. Forum. Trans. Tech. Publ. 321–324.
Brown, A.A., Bammann, D.J., 2012. Validation of a model for static and dynamic recrystallization in metals. Int. J. Plast. 32–33, 17–35.
Buken, H., Kozeschnik, E., 2017. A model for static recrystallization with simultaneous precipitation and solute drag. Metall. Mater. Trans. A 48, 2812–2818.
Cahn, R.W., Haasen, P., 1983. Physical Metallurgy. North-Holland, Amsterdam.
Cho, H., Hammi, Y., Bowman, A., Karato, S.-i., Baumgardner, J., Horstemeyer, M., 2019. A unified static and dynamic recrystallization Internal State Variable (ISV) constitutive model coupled with grain size evolution for metals and mineral aggregates. Int. J. Plast. 112, 123–157.
Deschamps, A., Brechet, Y., 1998. Influence of predeformation and ageing of an Al–Zn–Mg alloy—II. Modeling of precipitation kinetics and yield stress. Acta Mater. 47, 293–305.
Doherty, R., Hughes, D., Humphreys, F., Jonas, J.J., Jensen, D.J., Kassner, M., King, W., McNelley, T., McQueen, H., Rollett, A., 1997. Current issues in recrystallization: a review. Mater. Sci. Eng., A 238, 219–274.
Dutta, B., Palmiere, E.J., Sellars, C.M., 2001. Modelling the kinetics of strain induced precipitation in Nb microalloyed steels. Acta Mater. 49, 785–794.
Dutta, B., Sellars, C.M., 1987. Effect of composition and process variables on Nb (C, N) precipitation in niobium microalloyed austenite. Mater. Sci. Technol. 3, 197–206.
Elwazri, A.M., Essadiqi, E., Yue, S., 2004. Kinetics of metadynamic recrystallization in microalloyed hypereutectoid steels. ISIJ Int. 44, 744–752.
Engberg, G., Lissel, L., 2008. A physically based microstructure model for predicting the microstructural evolution of a C-Mn steel during and after hot deformation. Steel Res. Int. 79, 47–58.
Friedel, J., 1964. Dislocations. Pergamon Press, Oxford, UK.
Frost, H.J., Ashby, M.F., 1982. Deformation Mechanism maps: the Plasticity and Creep of Metals and Ceramics. Pergamon press, Oxford.
Galindo-Nava, E., Perlade, A., Rivera-Díaz-del-Castillo, P., 2014. A thermostatistical theory for solid solution effects in the hot deformation of alloys: an application to low-alloy steels. Modell. Simul. Mater. Sci. Eng. 22, 015009.
Galindo-Nava, E., Rivera-Díaz-del-Castillo, P., 2012. A thermodynamic theory for dislocation cell formation and misorientation in metals. Acta Mater. 60, 4370–4378.
Galindo-Nava, E., Rivera-Díaz-del-Castillo, P., 2013. Thermostatistical modelling of hot deformation in FCC metals. Int. J. Plast. 47, 202–221.
Galindo-Nava, E., Rivera-Díaz-del-Castillo, P., 2014. Thermostastitical modelling of deformation twinning in HCP metals. Int. J. Plast. 55, 25–42.
Galindo-Nava, E., Sietsma, J., Rivera-Díaz-del-Castillo, P., 2012. Dislocation annihilation in plastic deformation: II. Kocks–Mecking analysis. Acta Mater. 60, 2615–2624.
Geise, J., Herzig, C., 1985. Lattice and grain boundary diffusion of niobium in iron. Int. J. Mater. Res. 76, 622–626.
Gladman, T., 1966. On the theory of the effect of precipitate particles on grain growth in metals. Proc. R. Soc. London, Ser. A 294, 298–309.
Hansen, S., Vander Sande, J., Cohen, M., 1980. Niobium carbonitride precipitation and austenite recrystallization in hot-rolled microalloyed steels. Metall. Trans. A 11, 387–402.
Hasegawa, T., Yakou, T., Kocks, U., 1982. Length changes and stress effects during recovery of deformed aluminum. Acta Metall. 30, 235–243.
Hashmi, S., 2014. Comprehensive Materials Processing. Newnes.
He, D.-.G., Lin, Y., Chen, M.-.S., Li, L., 2017. Kinetics equations and microstructural evolution during metadynamic recrystallization in a nickel-based superalloy with δ phase. J. Alloys Compd. 690, 971–978.
Heidarzadeh, A., Zavašnik, J., Shabadi, R., Mousavian, R.T., 2021. Dynamic recrystallization's role in strength-ductility trade-off in polycrystalline Fe–Cr–Ni stainless steels produced by laser powder bed fusion. Mater. Sci. Eng., A 814, 141214.
Huang, M., Perlade, A., Rivera-Díaz-del-Castillo, P.E., 2011. Predicting the evolution of dislocation density following hot deformation. Philos. Mag. Lett. 91, 387–393.
Humphreys, F., 1997. A unified theory of recovery, recrystallization and grain growth, based on the stability and growth of cellular microstructures—I. The basic model. Acta Mater. 45, 4231–4240.
Humphreys, F.J., Hatherly, M., 2012. Recrystallization and Related Annealing Phenomena. Elsevier.
Hurley, P., Humphreys, F., 2003. Modelling the recrystallization of single-phase aluminium. Acta Mater. 51, 3779–3793.
Karjalainen, L., Perttula, J., Xu, Y., Niu, J., 1997. In: . National Research Institute for Metals, Tsukuba, Japan.
Kassner, M.E., 2018. Application of the Taylor Equation to Five-Power-Law Creep Considering the Influence of Solutes. Metals (Basel) 8, 813.

Li, H., Lin, J., Dean, T., Wen, S., Bannister, A., 2009. Modelling mechanical property recovery of a linepipe steel in annealing process. Int. J. Plast. 25, 1049–1065.
Li, Z., Li, Z., Tan, Z., Xiong, D.-.B., Guo, Q., 2020. Stress relaxation and the cellular structure-dependence of plastic deformation in additively manufactured AlSi10Mg alloys. Int. J. Plast. 127, 102640.
Liu, P., Wang, Z., Xiao, Y., Lebensohn, R.A., Liu, Y., Horstemeyer, M.F., Cui, X., Chen, L., 2020. Integration of phase-field model and crystal plasticity for the prediction of process-structure-property relation of additively manufactured metallic materials. Int. J. Plast. 128, 102670.
Martınez-de-Guerenu, A., Arizti, F., Gutiérrez, I., 2004. Recovery during annealing in a cold rolled low carbon steel. Part II: modelling the kinetics. Acta Mater. 52, 3665–3670.
Maugis, P., Gouné, M., 2005. Kinetics of vanadium carbonitride precipitation in steel: a computer model. Acta Mater. 53, 3359–3367.
Medina, S.F., Valles, P., Calvo, J., Cabrera, J.M., 2020. Nucleation and Growth of Precipitates in a V-Microalloyed Steel According to Physical Theory and Experimental Results. Phys. Met. Metallogr. 121, 32–40.
Miao, C., Shang, C., Zhang, G., Subramanian, S., 2010. Recrystallization and strain accumulation behaviors of high Nb-bearing line pipe steel in plate and strip rolling. Mater. Sci. Eng., A 527, 4985–4992.
Min, K., Jeong, W., Hong, S., Lee, C., Cha, P.-.R., Han, H., Lee, .M..-G., 2020. Integrated crystal plasticity and phase field model for prediction of recrystallization texture and anisotropic mechanical properties of cold-rolled ultra-low carbon steels. Int. J. Plast. 127, 102644.
Momeni, A., Ebrahimi, G., Jahazi, M., Bocher, P., 2014. Microstructure evolution at the onset of discontinuous dynamic recrystallization: a physics-based model of subgrain critical size. J. Alloys Compd. 587, 199–210.
Mukherjee, M., Prahl, U., Bleck, W., 2014. Modelling the strain-induced precipitation kinetics of vanadium carbonitride during hot working of precipitation-hardened Ferritic–Pearlitic steels. Acta Mater. 71, 234–254.
Nes, E., 1995. Recovery revisited. Acta Metall. Mater. 43, 2189–2207.
Nes, E., 1997. Modelling of work hardening and stress saturation in FCC metals. Prog. Mater Sci. 41, 129–193.
Nes, E., Ryum, N., Hunderi, O., 1985. On the Zener drag. Acta Metall. 33, 11–22.
Okaguchi, S., Hashimoto, T., 1992. Computer model for prediction of carbonitride precipitation during hot working in Nb-Ti bearing HSLA steels. ISIJ Int. 32, 283–290.
Perez, M., Dumont, M., Acevedo-Reyes, D., 2008. Implementation of classical nucleation and growth theories for precipitation. Acta Mater. 56, 2119–2132.
Perrard, F., Deschamps, A., Maugis, P., 2007. Modelling the precipitation of NbC on dislocations in α-Fe. Acta Mater. 55, 1255–1266.
Puchi-Cabrera, E., Staia, M., Guérin, J.-.D., Lesage, J., Dubar, M., Chicot, D., 2014. An experimental analysis and modeling of the work-softening transient due to dynamic recrystallization. Int. J. Plast. 54, 113–131.
Russell, K.C., 1980. Nucleation in solids: the induction and steady state effects. Adv. Colloid Interface Sci. 13, 205–318.
Sabzi, H.E., Aboulkhair, N.T., Liang, X., Li, X.-.H., Simonelli, M., Fu, H., Rivera-Díaz-del-Castillo, P., 2020. Grain refinement in laser powder bed fusion: the influence of dynamic recrystallization and recovery. Mater. Des. 196, 109181.
Sabzi, H.E., Hernandez-Nava, E., Li, X.-.H., Fu, H., San-Martín, D., Rivera-Díaz-del-Castillo, P.E., 2021. Strengthening control in laser powder bed fusion of austenitic stainless steels via grain boundary engineering. Mater. Des., 110246
Sakai, T., Belyakov, A., Kaibyshev, R., Miura, H., Jonas, J.J., 2014. Dynamic and post-dynamic recrystallization under hot, cold and severe plastic deformation conditions. Prog. Mater Sci. 60, 130–207.
Sakai, T., Ohashi, M., Chiba, K., Jonas, J., 1988. Recovery and recrystallization of polycrystalline nickel after hot working. Acta Metall. 36, 1781–1790.
Saxena, V., Krief, M., Adam, L., 2018. Handbook of Borehole Acoustics and Rock Physics for Reservoir Characterization. Elsevier.
Song, X., Rettenmayr, M., Müller, C., Exner, H.E., 2001. Modeling of recrystallization after inhomogeneous deformation. Metall. Mater. Trans. A 32, 2199–2206.
Svoboda, J., Fischer, F.D., Leindl, M., 2011. Transient solute drag in migrating grain boundaries. Acta Mater. 59, 6556–6562.
Tang, J., Jiang, F., Luo, C., Bo, G., Chen, K., Teng, J., Fu, D., Zhang, H., 2020. Integrated physically based modeling for the multiple static softening mechanisms following multi-stage hot deformation in Al-Zn-Mg-Cu alloys. Int. J. Plast. 134, 102809.
Tang, X., Wang, B., Ji, H., Fu, X., Xiao, W., 2016. Behavior and modeling of microstructure evolution during metadynamic recrystallization of a Ni-based superalloy. Mater. Sci. Eng., A 675, 192–203.
Uranga, P., Fernandez, A., Lopez, B., Rodriguez-Ibabe, J., 2003. Transition between static and metadynamic recrystallization kinetics in coarse Nb microalloyed austenite. Mater. Sci Eng.: A 345, 319–327.
Vasilyev, A., Sokolov, S., Kolbasnikov, N., Sokolov, D., 2011. Effect of alloying on the self-diffusion activation energy in γ-iron. Phys. Solid State 53, 2194–2200.
Verdier, M., Brechet, Y., Guyot, P., 1998. Recovery of AlMg alloys: flow stress and strain-hardening properties. Acta Mater. 47, 127–134.
Vohringer, O., 1987. Relaxation of Residual Stresses by Annealing or Mechanical Treatment. Pergamon Press, Oxford.
Wang, H., Wang, J., Tong, Z., Hodgson, P., Wan, X., Wu, K., Wei, R., Timokhina, I., 2018. Characterization of Nb interface segregation during welding thermal cycle in microalloyed steel by atom probe tomography. Metall. Mater. Trans. A 49, 6224–6230.
Winning, M., Gottstein, G., Shvindlerman, L., 2001. Stress induced grain boundary motion. Acta Mater. 49, 211–219.
Winning, M., Rollett, A., Gottstein, G., Srolovitz, D., Lim, A., Shvindlerman, L., 2010. Mobility of low-angle grain boundaries in pure metals. Philos. Mag. 90, 3107–3128.
Xu, T., 1997. Non-equilibrium cosegregation to grain boundaries. Scripta Mater. 37, 1643–1650.
Zener, C., 1949. Theory of growth of spherical precipitates from solid solution. J. Appl. Phys. 20, 950–953.
Zeng, R., Huang, L., Li, J., Li, H., Zhu, H., Zhang, X., 2019. Quantification of multiple softening processes occurring during multi-stage thermoforming of high-strength steel. Int. J. Plast. 120, 64–87.
Zhang, J., Huo, C., Ma, Q., Feng, Y., 2018. NbC-TiN co-precipitation behavior and mechanical properties of X90 pipeline steels by critical-temperature rolling process. Int. J. Pres. Ves. Pip. 165, 29–33.
Zhang, Z., Liu, Y., Liang, X., She, Y., 2008. The effect of Nb on recrystallization behavior of a Nb micro-alloyed steel. Mater. Sci. Eng., A 474, 254–260.
Zhao, J., Wang, X., Quan, Y., Wang, Q., Song, G., 2018. High precision shape model and presetting strategy for strip hot rolling. J. Mater. Process. Technol. 265.
Zouari, M., Loge, R.E., Beltran, O., Rousselle, S., Bozzolo, N., 2014. Multipass forging of inconel 718 in the delta-Supersolvus domain: assessing and modeling microstructure evolution. In: MATEC Web of Conferences. EDP Sciences, p. 12001.
Zurob, H., 2003. Effects of precipitation, Recovery and Recrystallization On the Microstructural Evolution of Microalloyed Austenite. McMaster University, Ontario, Canada.
Zurob, H., Brechet, Y., Dunlop, J., 2006. Quantitative criterion for recrystallization nucleation in single-phase alloys: prediction of critical strains and incubation times. Acta Mater. 54, 3983–3990.
Zurob, H., Brechet, Y., Purdy, G., 2001. A model for the competition of precipitation and recrystallization in deformed austenite. Acta Mater. 49, 4183–4190.
Zurob, H., Hutchinson, C., Brechet, Y., Purdy, G., 2002. Modeling recrystallization of microalloyed austenite: effect of coupling recovery, precipitation and recrystallization. Acta Mater. 50, 3077–3094.